Transactions, SMiRT-22
San Francisco, California, USA - August 18-23, 2013
Division II

CHARACTERISATION OF THE DUCTILE FRACTURE MECHANISM IN A508 CLASS 3 REACTOR PRESSURE VESSEL STEEL USING LABORATORY X-RAY TOMOGRAPHY IMAGING

Michael Daly[1], Fabien Leonard[2], John K. Sharples[3] and Andrew H. Sherry[4]

[1]Research Engineer (EngD), Materials Performance Centre, University of Manchester, The Mill, Sackville Street Manchester, M13 1QD, UK
[2]Henry Moseley X-ray Imaging Facility, School of Materials, The University of Manchester , Materials Science Centre, Grosvenor Street, Manchester, M13 9PL, UK
[3]Team Leader and Consultant, Structural Integrity at AMEC, Walton House, Birchwood Park, Warrington, Cheshire, WA3 6AT, UK
[4]Professor, Dalton Nuclear Institute, University of Manchester, Pariser Building – G Floor, Sackville Street, Manchester, M13 9PL, UK

ABSTRACT

Reactor pressure vessels (RPV) are manufactured from medium strength low allow ferritic steel specifically selected for its high toughness and weldability. The ability of the RPV to withstand crack propagation is crucial to maintaining the operational safety of the reactor plant. The normal operating temperature of current generations of RPV steels is sufficiently high to ensure that the material remains ductile during its service life. Furthermore, new materials are engineered to exhibit greater ductility and fracture toughness throughout their operating life. Therefore understanding and being able to predict the ductile fracture behaviour is critical for assuring the safety of RPV steels during operating conditions.

Ductile damage is characterised by the nucleation, growth and coalescence of voids at initiating particles within the volume of high triaxial stresses ahead of a crack-tip or stress concentrator. The crack propagates once a critical void volume fraction has been attained. Predictive mechanistically based models such as the Gurson-Tvergaard-Needleman (GTN) model require calibration against material data. This is conventionally undertaken by fitting the model to fracture toughness data generated from notched or pre-cracked specimens. However, modern microstructural characterisation techniques are opening up new approaches for model calibration which utilise 3D quantification of void volume fractions during damage evolution and final fracture.

This paper demonstrates a functional method of using laboratory X-ray tomography imaging for characterising and quantifying the void distribution and critical void volume fraction below the fracture surface of pre-cracked compact test specimens manufactured from A508 Class 3 RPV steel tested to failure at ambient temperature.

INTRODUCTION

The mechanism of ductile fracture is characterised by the nucleation, growth and coalescence of voids at initiating particles. These particles are categorised as inclusions and second phase particles, and in ferritic steel are most often manganese sulphide (MnS) inclusions and metallic carbide particles (M_nC). The voids form at these particles within the volume of high plastic strain and triaxial stresses ahead of a crack-tip or stress concentrator.

Two nucleating processes have been observed (Van Stone, et al., 1985): void formation by either decohesion of the interface between the matrix and the inclusion/particle, or by cracking of the inclusion/particle itself. Voids then grow under the influence of increasing plastic strain and high hydrostatic stress within the material. A crack will propagate once neighbouring voids coalesce and/or

reach a critical size producing a macroscopic flaw. The coalescence of the voids can be considered as the final stage in the crack growth mechanism.

The larger particles nucleate voids at lower stresses and strains (Everett, et al., 2001). Smaller particles will start contributing to void nucleation when the material is subjected to greater plastic deformation. The nucleation of voids at smaller particles, often between larger voids or microcracks where intense shear occurs, may result in a void sheeting effect further contributing to void coalescence (Pardoen & Hutchinson, 2000 and Tvergaard, 1982).

The metallurgical characteristics of the microstructure, including the size and distribution of the initiating particles which can often concentrate close to or on the grain boundaries, will contribute to the nucleation and coalescence process. The distribution of these particles may also be heterogeneous within the material with regions with a greater concentration of particles or varying grain sizes (Thomson, et al., 2003).

There exists a range of mathematical models that have been developed to describe the ductile fracture process. One of these is the Gurson-Tvergaard-Needleman (GTN) (Zhang, 2001) model which introduces a yielding criterion that is partly dependent on a critical void volume fraction which is driven by the nucleation of new voids, the growth of new and initial voids within the material and the coalescence of voids.

The accuracy of the GTN model relies on material specific data obtained from microstructural analysis and standard fracture test specimens as well as being dependent on the mesh used for the finite element analysis. The initial void volume fraction is determined by analysing the bulk material or by using the Franklin formula (Franklin, 1969) for spherical inclusions which considers the weight percent of Manganese and Sulphide elements to determine the initial void nucleation sites. The critical void volume fraction is obtained from fracture tests of standardised test specimens. The length of the elements at the crack tip is defined by the inter-particle spacing. This has been typically obtained by successively polishing the metallic surface to reveal the distribution of the particles. Additionally, guidance from the R6 procedure (R6 - Rev 4, 2009) advises on standard elements lengths ranging between 125µm to 800µm for A508 Class 3 ferritic steel.

Previous experiments have shown that the void volume fractions (VVF) may vary by material but also by specimen types. Taylor et al, 2012 and Daly et al, 2012 have shown that the VVF will vary as a function of the fracture test specimen used for testing aluminium samples and A508 class 3 samples respectively. For aluminium, the pre-cracked compact test (CT) specimens have a higher concentration of voids very close to the fracture surface when compared with notched tensile specimens. On the other hand, the voids extend further below the fracture surface for notched tensile specimens than pre-cracked specimens. Furthermore, recent experiments on A508 Class 3 CT fracture samples have shown that the voids can extend well below the fracture surface as a result of the distribution of large initiating particles.

The aim of this paper is to propose a method for quantifying and analysing the ductile damage below a fracture surface by using X-ray tomography to obtain the fitting parameters required for calibrating the GTN model for A508 Class 3 ferritic steel. This method allows for the estimation of the average diameter size of the voids as well as their distribution from the fracture surface and the distance to their nearest neighbour.

EXPERIMENTAL

Material

The material used throughout this experiment was an A508 Class 3 ferritic steel. The specimens were extracted from the outer ring of an upright wedge-shaped block originating from a larger ring forging. All the specimens were extracted from the same location and in the same orientation. The chemical composition (wt%) of the ferritic steel was evaluated using spectographic analysis and the results are indicated in Table 1.

Table 1: Chemical composition in wt% of A508 Class 3 Steel.

C	Si	Mn	P	S	Cr	Mo	Ni	Al	Co	Cu	Sn	Ti	V
0.18	0.23	1.3	<0.005	<0.005	0.25	0.55	0.81	0.02	0.01	0.04	0.005	<0.01	0.01

Mechanical testing

The tensile properties of the material were determined on standard round-bar test specimens oriented in the hoop direction. Three tensile specimens were tested on a Zwick 1464 at room temperature using a strain rate of 0.025% s-1 according to BS EN ISO 6892 procedure.

Ten fracture toughness tests were performed according to the ESIS P2-92 standard using CT specimens with standard dimensions of thickness, B = 25mm, width, W = 50mm and a crack length to specimen width ratio, a/W = 0.5. Specimens were 20% side-grooved following fatigue pre-cracking. Tests were performed using both the unloading compliance and the multi specimen methods. Out of the ten compact test specimens, two were left intact in order to preserve the crack tip for analysis.

Metallographic Analysis

The cracked and parent material was imaged using optical and scanning electron microscopes. The parent material was imaged to characterise the general microstructure of the ferritic steel with a specific interest on grain sizes and particle and inclusion distribution. The cracked specimens were analysed to characterise the ductile fracture mechanism.

For the parent material, metallographic sections were taken to view the material in the axial-radial plane. The fractured sections were machined through the fractured specimen halves in the region where plain strain fracture was expected to take place. The metallographic sections were progressively ground and polished to a mirror finish of 0.25 μm using diamond paste and etched using colloidal silica and 2% Nital.

X-ray Tomography Analysis

The test samples for X-ray tomography imaging were machined below the fracture surface of three CT specimens using electrical discharge machining (EDM). The samples were extracted at regular intervals starting at the pre-cracked region but before the initiation of ductile tearing. The remaining specimens were extracted from below the ductile crack path and beyond the crack arrest point. The sections were extracted as close as possible to the region where plane strain was expected to take place with the greatest amount of ductile tearing damage. The samples were approximately 0.5mm in diameter and 12mm in length, dimensions comparable to mechanical pencil lead refills. The surfaces of these small cylinders were lightly polished to remove any rust or scaling resulting from the EDM.

The top 4mm very close to the fracture surface of these specimens were scanned at the Henry Moseley X-ray Imaging Facility on the Nikon Metrology 225/320 kV Custom Bay system equipped with a 225 kV static multi-metal anode source and a PerkinElmer 2000 × 2000 pixels 16-bit amorphous silicon flat panel detector.

The scanning was performed with a molybdenum target using a voltage of 80 kV and a current of 130 μA. The data acquisition was carried out with an exposure time of 1000 ms, and no filtration. The

number of projections was set to 3142 and the number of frames per projection was 1. The entire volume was reconstructed at full resolution with a voxel size of 2.0 µm along the x, y, and z directions.

The data processing was performed with Avizo® Fire 7.0 software. An edge preserving smoothing filter was applied to the raw data to reduce image noise in each data set. Standard data processing was used to determine the void size distribution whereas a methodology similar to Leonard, et al, 2012 was employed to determine the void to fracture surface distance and evolution of void volume fraction.

Quantification and Analysis of Ductile Tearing

Using the Avizo® Fire data, the void volume fraction was estimated by measuring the voxel counts of metallic voxels against the count of porous voxels below the fracture surface. The VVF was calculated for each regions of interest (ROI). A ROI of 100µm in height was utilized to break the specimens into smaller cylinder regions which were comparable to the units used in Daly et al, 2012. The VVF was calculated for the specimens originating below the pre-cracked surface as well as the region below the ductile tearing surface and beyond the crack arrest.

Additionally, the average diameter of each void and their location with regards to each other within the sample volume was estimated. As the voxel resolution is 2µm, only voids with three times or more this dimension were accounted for as three voxels are usually required to visualise an object with a certain degree of confidence. The distance between a void's first neighbour was also measured for all voids greater than 6µm.

RESULTS

The results from the three tensile tests at room temperature are summarised in Table 2. The average yield stress was 446 MPa and the ultimate tensile stress was 594 MPa.

The fracture toughness properties of the A508 Class 3 steel are illustrated as a J R-curve in Figure 1 which includes data from both the unloading compliance tests and monotonically loaded tests presented together. The data from both test types are in agreement and the initiation toughness, measured by the intersection of the blunting line including 0.2 mm tearing and the power-law curve fit to the data is ~ 475 kJ/m^2. The specimens for tomography analysis were extracted from test samples B, G and C as these specimens were subjected to the most ductile tearing.

Table 2 (Left): A508 Cl 3 Mechanical Properties

Specimen No.	T1	T2	T3	Average
Modulus (GPa)	211	210	208	210
0.2% proof stress (MPa)	455	457	436	446
1.0% proof stress (MPa)	458	467	450	458
Ultimate tensile stress (MPa)	595	602	586	594
Elongation (%)	29	27	27	28
Reduction in Area (%)	75	75	74	75

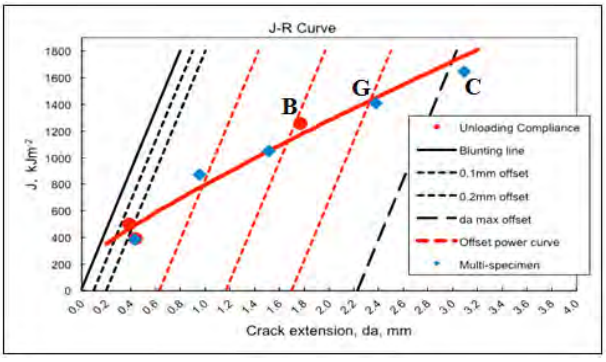

Figure 1 (Right): J-R Curve for A508 Cl 3 material tested in the hoop-radial direction at 23°C.

Figure 2a and 2b illustrate the general upper bainitic microstructure of the A508 Class 3 RPV ferritic steel under the optical microscope and SEM respectively. The average grain size was estimated at 11µm. But the microstructure is interspersed with clusters of very small grains and regions where very large grains are present.

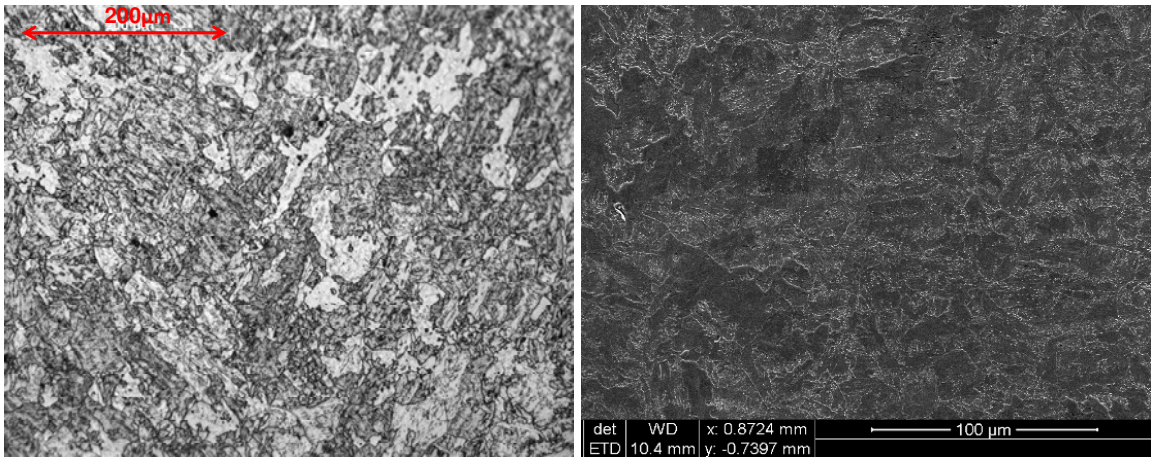

Figure 2a & 2b: General microstructure of the upper bainitic steel under optical microscope (left) and SEM (right).

Figure 3a and 3b show the microstructural characterisation of the ductile tearing process in A508 class 3 ferritic steel. Microvoids were observed to initiate and grow by the decohesion of carbides from the matrix. Larger voids, in some cases, were shown to nucleate at proximity to large particles. These larger voids were observed to be present well below the fracture surface and extending ahead of the crack tip.

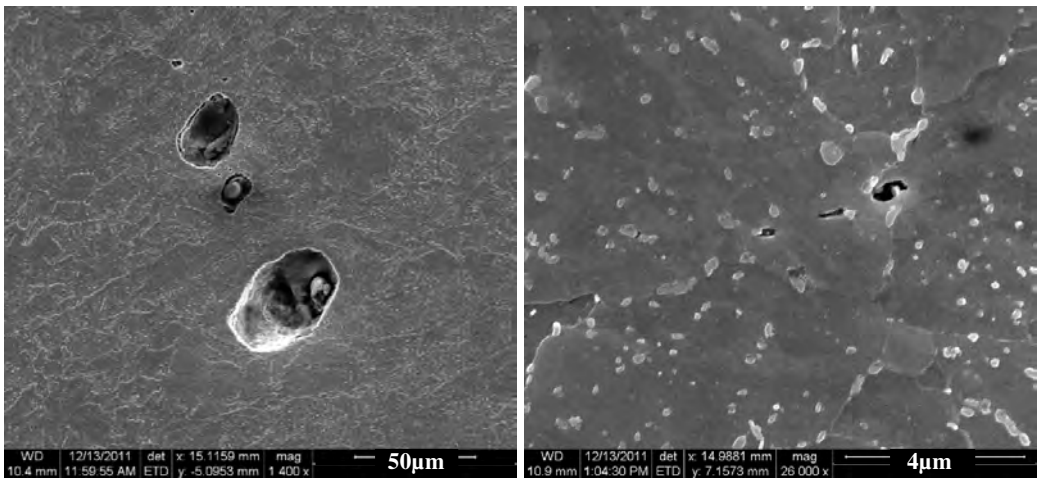

Figure 3a & 3b: SEM images of large macroscopic voids with large inclusion (left) and microvoids nucleating at proximity to carbides very close to the fracture surface (right).

X-ray Tomography

The X-ray tomography images of Figure 4 shows the typical distribution of voids below the fracture surface for a specimen extracted from below the crack path. Voids as little as 6µm in diameter could realistically be resolved with a certain degree of confidence. The ability to use the X-ray tomography technique enabled the imaging of voids in their entirety. As a result, some voids are observed to have elongated shapes further suggesting the coalescence mechanism of ductile tearing. Furthermore, this technique demonstrated the ability to visualise and quantify voids and in some cases, clusters of voids up to 3.6mm below the fracture surface.

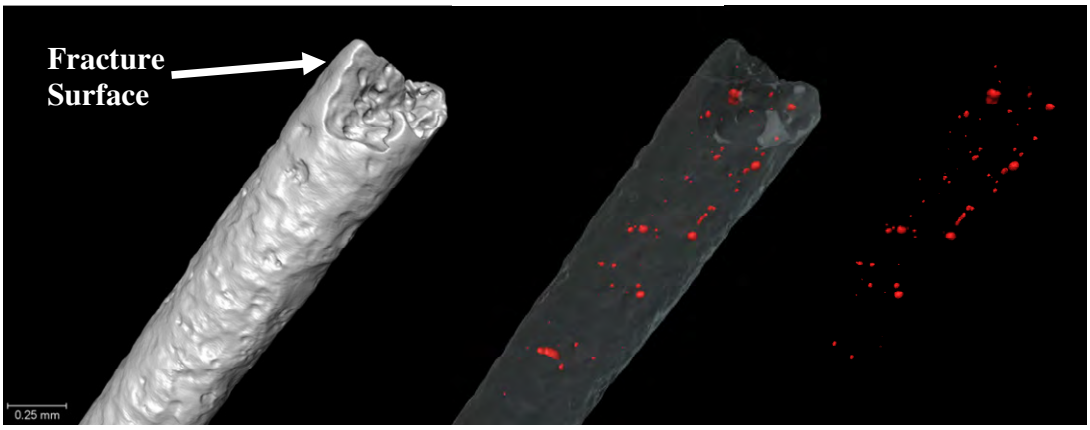

Figure 4: 3D tomographic image of the ferritic steel samples and the void distribution below the fracture surface.

Quantification Results

The variation of the void volume fraction as a function of distance below the fracture surface in the CT specimens is illustrated in Figure 5. The data was calculated by quantifying the average VVF for cylindrical cells of 100µm in height and starting from the fracture surface. The VVF for each specimen location (0mm, 0.5mm, 1mm, 2mm, 3mm and beyond crack-tip) was averaged over all three specimens (B, C and G) to obtain an average VVF for the first 100µm below the fracture surface and every 100µm down to 3.6mm.

The crack arrest location of the fracture toughness tests was also taking into consideration. Samples B and G had crack extensions of approximately 2mm, the extractions beyond the crack front were averaged separately and labeled as “beyond crack-tip” on the plot.

The critical void volume fraction peaks at a maximum of 0.975×10^{-2} for the measurements from the 2mm crack tearing extraction. The greatest number of voids is quantified within the first 800µm below the fracture surface. Secondary VVF peaks are observed well below the fracture surface which is characteristics of clusters of voids and very large voids nucleating at lower strains. The results for this plot have been further discussed in Daly, et al., 2013.

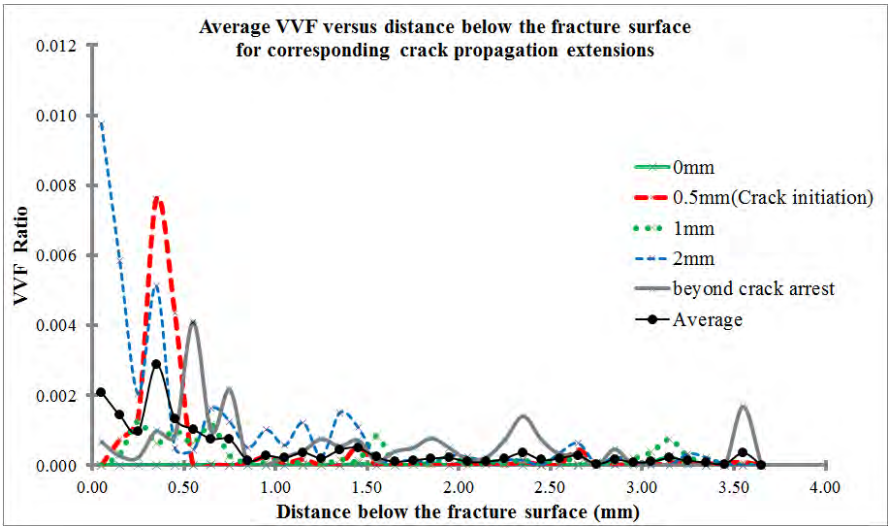

Figure 5: VVF as a function fo distance below the fracture surface.

The distribution of the average void diameter is shown in Figure 6. On average, the void diameters range primarily from 6µm to 30µm in diameter and peaks with most voids measuring between 11µm and 20µm in diameter.

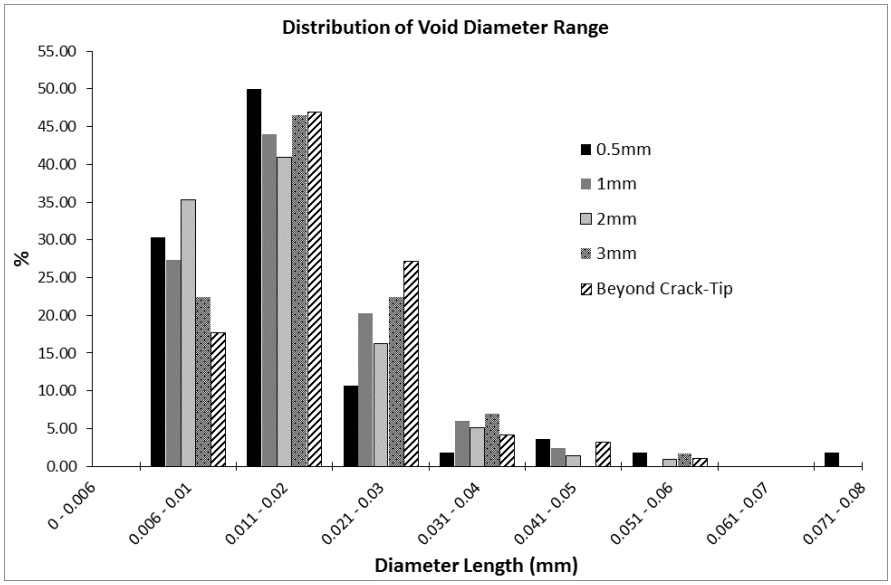

Figure 6: Histogram of the range of void diameters quantified using X-ray Tomography.

The data from Figure 7 shows the broad distribution in the distance between the void's first neighbour. The distance between voids peaks between 45µm and 90µm. The distribution does not take into consideration the relative distance from the fracture surface where the distance between voids might increase further below the fracture surface. But according to Figure 5, the majority of voids are located within 1mm below the fracture surface which should be sufficiently representative.

Finally, the X-ray imaging equipment was limited in the size of voids it could accurately resolve. Scanning electron microscope images very close to the fracture surface showed a great number of voids in close proximity to each other and in the range of 1µm to 6µm in diameter. These additional voids were not quantified for this quantification exercise.

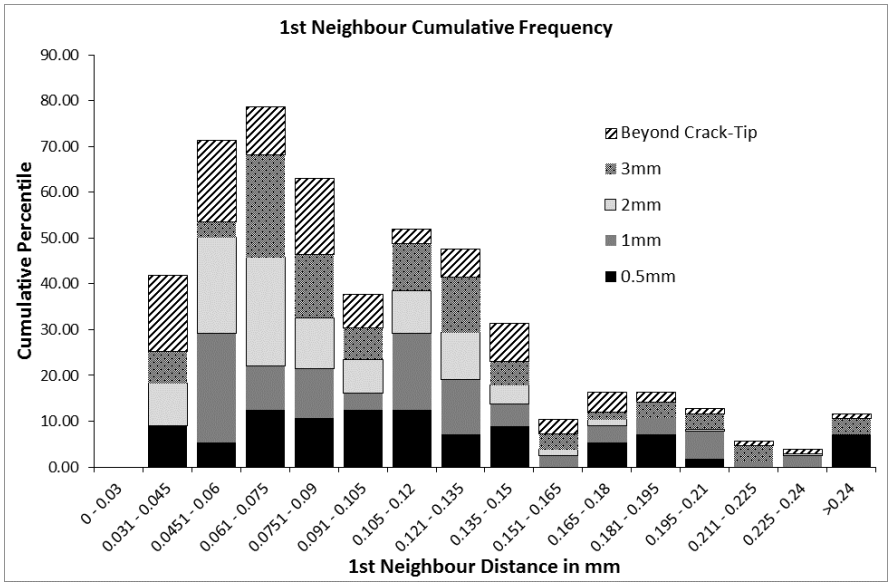

Figure 7: Histogram of the range of the spacing between voids.

DISCUSSION

The void volume fraction measured for the A508 class 3 compares favourably with results obtained for aluminium compact test specimens. Previous results from Taylor et al, 2012 obtained a void volume fraction f_f of approximately 1.1×10^{-2} for the aluminium alloy compared to $f_f = 0.975\times10^{-2}$ for the RPV ferritic steel. Additionally, the steel exhibits peaks in the VVF well below the fracture surface. These are often a result of large voids or clusters of voids. Everett et al, 2001 have shown that the distribution of voids deep below the fracture surface was attributed to microstructural banding and larger MnS inclusions in HY100 Steel. These larger MnS inclusions preferentially promote the nucleation of voids at relatively low strains.

Previous work by Thomason, 1998 has shown that the dimension and spacing of the voids will lead to large variations in the ductile fracture strains for various void volume fractions and stress states. The plastic limit load model considers the size and spacing of the voids in order to describe the fracture behaviour as either a homogeneous or localized deformation mode that will ultimately lead to the collapse of the matrix ligament and the coalescence of voids. The tomography results have shown a wide range of void sizes and spacing with peak void diameters between 10µm and 20µm and void spacing ranging between 45µm and 90µm. The variation in the void population size and spacing indicates the suitability to consider a multiple and/or statistical void nucleation model to the dual-plasticity nature of the plastic limit load model within the GTN model.

Furthermore, the tomography results have shown a disparity between the recommended values of the R6 procedure for f_0, f_c and L as shown in Table 3. The value of f_0 of 0.00023 was estimated using the Franklin formula but the peaks observed in Figure 5 would ultimately increase the f_0 beyond the recommended R6 values of 0.0001 and 0.00016. The critical VVF of the tomography results has been shown to be within similar values or larger than the R6 values depending on the location of the

extractions. The variability of the final VVF for the tomography is a result of the uneven and jagged surface of the fracture surface slightly skewing the actual distance below the fracture surface.

Finally, the L spacing that defines the length of the finite elements which is derived from the inter-particle spacing is substantially smaller for the tomography results. It is worth noting that the tomography results provide the spacing between voids but the inter-dependency of voids nucleating near nucleating particles is relevant. Furthermore, the void spacing is comparable with previous work from Beremin, 1981 on A508 Class 3 steel where the inter-particle spacing was estimated to be 60µm.

Table 3: Comparison between R6 Gurson model parameters and X-ray tomography results.

A508 Class 3 CT specimens	L µm	f_0	f_c
R6	800	0.0001	0.005
R6	800	0.00016	0.003
R6	125	0	0.004
Tomography	45 ≤ L ≤ 90	≈ 0.00023	max = 0.00975

Further work will aim to use synchrotron X-rays to image and quantify the smaller voids at proximity to the fracture surface in order to improve the statistical range of the void sizes and spacing. Furthermore, the phase contrast imaging capability of a synchrotron source to image large inclusions within the samples will contribute to confirm that the imaging of the voids is a suitable alternative to quantifying the distribution of nucleating particles.

CONCLUSION

This paper has demonstrated the analytical and quantifiable capabilities of X-ray tomography imaging in order to characterise the ductile damage in A508 Class 3 RPV steel. The main conclusions of this work are as follows:

- The ductile fracture mechanism was identified to occur by the decohesion of the matrix from inclusions and second phase particles.
- The ductile tearing damage was successfully imaged and quantified using X-ray laboratory sources to image voids of approximately 6µm in diameter and larger below the crack surface of compact test specimens.
- The main parameters to calibrate the GTN models were successfully acquired. The initial and critical VVF were quantified and the average void diameters and spacing were measured. Some disparity exists between the recommended values of the R6 procedure and the tomography results.
- The distribution of void spacing obtained from tomography is closely comparable to the average inter-particle spacing observed by Beremin, 1981 in A508 Class 3 RPV steel.

Acknowledgements

The authors are grateful to AMEC in Risley for their support in the use of their material testing and microscopy equipment, and to Tristan Lowe from the University of Manchester Henry Moseley X-ray Imaging Facility for the use of the machines and expertise.

REFERENCES

Beremin, F. M., 1981. Cavity Formation from inclusions in Ductile Fracture in A508 Steel. *American Society for Metals and the Metallurgical Society of AIME,* Volume 12A, pp. 723-731.

British Standards, n.d. *Metallic materials. Tensile Testing. Method of test at ambient temperature,* s.l.: BS EN ISO 6892-1:2009.

Daly, M., Leonard, F., Sharples, J. K. & Sherry, A. H., 2013. *Advanced assessment of Ductile Tearing in Nuclear reactor Pressure Vessel Steel Using X-ray Tomography.* Beijing, International Conference on Fracture (ICF13).

Daly, M., Sharples, J. K. & Sherry, A. H., 2012. *Advanced Assessment of the Integrity of Ductile Components.* Toronto, s.n.

European Structural Integrity Society, 1992. *ESIS Standard No. P2-92: Procedure for determining the fracture behaviour of materials,* s.l.: ESIS.

Everett, R. K., Simmonds, E, K. & Geltmacher, A. B., 2001. Spatial Distribution of Voids in HY-100 Steel by X-Ray Tomography. *Scripta Materialia,* Volume 44, pp. 165-169.

Franklin, A. G., 1969. Comparison between a quantitative microscope and chemical methods for assessment of non-metallic inclusions.. *Iron and Steel Inst,* Volume 207, pp. 181-186.

Leonard, F., Stein, J., Wilkinson, A. & Withers, P., 2012. *3D Characterisation of Void Distribution in Resin Film Infused Composites.* s.l., s.n.

Pardoen, T. & Hutchinson, J. W., 2000. An extended model for void growth and coalescence. *Journal of the Mechanics and Physics of Solids,* Volume 48, pp. 2467-2512.

R6 - Rev 4, 2009. *Chapter III Section 9: Guidance on use of local approach,* s.l.: BEGL.

Taylor, K. L. & Sherry, A. H., 2012. The characterisation and interpretation of ductile fracture mechanisms in AL2024-T351 using X-ray and focused ion beam tomography. *Acta Materialia,* Volume 60, pp. 1300-1310.

Thomason, P. F., 1998. A View on Ductile-Fracture Modelling. *Fatigue and Fracture of Engineering Materials & Structures,* Volume 21, pp. 1105-1122.

Thomson, C. I. A., Worswick, M. J., Pilkey, A. K. & Lloyd, D. J., 2003. Void coalescence within periodic clusters of particles. *Journal of the Mechanics and Physics of Solids,* Volume 51, pp. 127-146.

Tvergaard, V., 1982. Ductile fracture by cavity nucleation between larger voids. *Journal of the Mechanics and Physics of Solids,* Volume 30, pp. 265-286.

Van Stone, R. H., Cox, T. B., Low Jr, J. R. & Psioda, J. A., 1985. Microstructural aspects of fracture by dimpled rupture. *International Metals Reviews,* Volume 30 No 4, pp. 157-179.

Zhang, Z. L., 2001. A complete Gurson Model. *Non Linear Fracture and Damage Mechanics,* pp. 223-248.